Chemical Science

ROYAL SOCIETY OF CHEMISTRY

EDGE ARTICLE

View Article Online
View Journal

Cite this: DOI: 10.1039/d5sc09030j

All publication charges for this article have been paid for by the Royal Society of Chemistry

Revisiting high-valence dopant mechanisms in Ni-rich cathodes: cation ordering dominates over morphological alignment for enhanced stability

Shuo Wang,†[a] Siqi Chen,†[a] Xiaohong Liu,*[a] Guilin Feng,[b] Bin Zhang,[c] Wangyan Xing,[c] Yao Xiao,*[d] Hao Liu*[e] and Wei Xiang*[afg]

Received 19th November 2025
Accepted 5th December 2025

DOI: 10.1039/d5sc09030j

rsc.li/chemical-science

Layered ultra-high-nickel oxides are promising cathodes for high-energy-density lithium-ion batteries but suffer from severe structural degradation. Although high-valence doping is widely employed to enhance stability, the underlying mechanism—whether dominated by morphological alignment or cation ordering—remains contested. Through systematic investigation of W^{6+}-doped $LiNi_{0.92}Co_{0.04}Mn_{0.04}O_2$ across varied doping concentrations and sintering temperatures, this work demonstrates that cation ordering, rather than morphological alignment, plays the decisive role in electrochemical enhancement. Although W-doping refines primary particles and sustains a radial microstructure even under extreme sintering conditions (up to 850 °C), correlation analysis reveals that cycling stability and specific capacity depend strongly on the suppression of Li^+/Ni^{2+} cation mixing, while showing only weak correlation with grain morphology. The 0.75 mol% W doped cathode calcined at 800 °C delivered a high specific capacity of 244.3 mAh g^{-1} and exceptional long-term cyclability, retaining 91.53% capacity after 1000 cycles in full cells. These findings clarify that high-valence dopants enhance performance primarily *via* lattice stabilization through cation ordering and highlight the necessity of co-optimizing doping content with synthesis temperature. This work revises the conventional understanding of high-valence doping mechanisms by establishing cation ordering as the primary factor for stability, providing a generalizable principle for designing next-generation ultra-high-nickel cathodes.

1. Introduction

Layered nickel-rich oxides ($LiNi_{1-x-y}Co_xMn_yO_2$, $x + y \leq 0.1$) represent state-of-the-art high-energy-density cathodes for lithium-ion batteries, delivering specific capacities exceeding 220 mAh g^{-1}. Their adoption is critically important for achieving the energy density targets required to extend the driving range of electric vehicles, which typically necessitate nickel contents exceeding 90%. However, the commercial implementation of these materials is challenged by intrinsic structural instabilities that become increasingly severe with higher Ni content. Delithiation beyond approximately 60% state-of-charge induces severe structural degradation, including anisotropic lattice contraction, the formation of intergranular microcracks, and oxidative decomposition of the electrolyte catalyzed by highly reactive Ni^{4+} species.[1] These interrelated failure mechanisms accelerate capacity fading and raise safety concerns, thereby limiting the practical application of ultra-high-Ni cathodes.

To mitigate these issues, two principal stabilization strategies have been developed. The first involves microstructural alignment.[1] Radially aligned, elongated primary particles constructed through a radially aligned precursor or dopant-assisted grain refinement could effectively dissipate mechanical strain, inhibit microcrack propagation, and shorten lithium-ion diffusion paths.[2] Seminal work by Sun *et al.* demonstrated that a radially aligned microstructure in Nb doped $LiNi_{0.938}Co_{0.041}Al_{0.021}O_2$ (NCA90) retains 88.3% capacity after 1000 cycles, owing to efficient strain accommodation.[3] More recently, high-valence dopants like Mn^{4+}, Sb^{5+}, Ta^{5+}, Mo^{6+}, and W^{6+} have been shown to segregate at grain boundaries, suppressing excessive particle growth during calcination and helping to maintain desirable needle-like primary particle morphologies over

[a]College of Materials and Chemistry & Chemical Engineering, Chengdu University of Technology, Chengdu 610059, China. E-mail: xhl@cdut.edu.cn; xiangwei@cdut.edu.cn

[b]Research Institute of Frontier Science, Southwest Jiaotong University, Chengdu 610031, PR China

[c]Yibin Libode New Materials Co., Ltd, Yibin 644200, PR China

[d]College of Chemistry and Materials Engineering, Wenzhou University, Wenzhou, 325035, PR China. E-mail: xiaoyao@wzu.edu.cn

[e]Institute for Applied Materials (IAM), Karlsruhe Institute of Technology, Hermann-von-Helmholtz-Platz 1, 76344 Eggenstein-Leopoldshafen, Germany. E-mail: yierliuhao@163.com

[f]Ruyuan HEC New Energy Materials Co., Ltd, Ruyuan 512700, PR China

[g]Tianfu Yongxing Laboratory, Chengdu 610213, PR China

† Shuo Wang and Siqi Chen contributed equally to this work and therefore share co-first authorship.

a broad sintering temperature range.[4–13] This controlled microstructure is widely recognized as a major factor contributing to the improved cycling stability of doped Ni-rich cathodes.[14] The second strategy focuses on lattice stabilization through high-valence cation doping.[4–6,15] The incorporation of cations with high oxidation states (*e.g.*, W^{6+}, Mo^{6+}, Nb^{5+}) strengthens the transition metal–oxygen (TM–O) bond, suppresses oxygen loss, and reduces Li^+/Ni^{2+} cation mixing.[5–7,16–18] For instance, W^{6+} doping in Ni-rich cathodes has been found to stabilize the host lattice, delaying phase transitions, and reducing the extent of *c*-axis contraction.[7,16,19–21] Additionally, such dopants promote the partial reduction of Ni^{2+} to maintain charge neutrality. This process may enhance cation ordering within the transition metal layer, a structural feature correlated with improved Li^+ diffusion kinetics and structural reversibility.

However, a critical paradox persists in the current understanding. While high-valence dopants concurrently improve morphological properties and lattice robustness, the predominant mechanism governing electrochemical stability remains debated. The prevailing literature predominantly highlights morphological alignment as the performance-limiting factor.[12,22–29] For instance, Park *et al.* argue that Nb^{5+}-induced grain refinement and radial alignment are decisive for the cyclability of $LiNi_{0.92}Co_{0.04}Mn_{0.04}O_2$, attributing a capacity retention of 90% after 500 cycles primarily to crack suppression.[23] Similarly, Mo^{6+} doping in $LiNi_{0.89}Mn_{0.1}Mo_{0.02}O_2$ results in ultra-fine grains (<200 nm) and exceptional mechanical resilience.[30] However, our earlier comparative study uncovered a notable contradiction: although the Mo-doped cathode exhibited more pronounced radial alignment and finer grains, its W-doped counterpart delivered significantly superior capacity retention.[30] Specifically, W^{6+} has a high charge density and strong M–O bonds, which are effective in suppressing cation disorder and stabilizing the layered structure. This inconsistency challenges the conventional paradigm that morphology optimization is the primary driver of performance. Instead, it suggests that lattice stabilization may play an underappreciated or even a dominant role, specifically through mechanisms that enhance cation ordering and improve the reversibility of phase transitions.[31] Further complexity arises from the interdependent effects of dopant concentration and synthesis temperature. On one hand, insufficient doping levels fail to mitigate cation disordering at elevated calcination temperatures, whereas excessive doping promotes the formation of resistive secondary phases that impair Li^+ transport. On the other hand, higher temperatures tend to promote grain coarsening yet may simultaneously enhance crystallinity and reduce cation mixing.[32,33] Thus, disentangling the respective contributions of morphological alignment *versus* intrinsic lattice stabilization requires systematically decoupling these co-varying parameters, a critical task that remains unaddressed in existing studies.

This study addresses the enduring debate regarding the key factors underlying the electrochemical stability of ultra-high-nickel layered oxide cathodes, through a systematic investigation of W^{6+}-modified $LiNi_{0.92}Co_{0.04}Mn_{0.04}O_2$. A full series of $Li(Ni_{0.92}Co_{0.04}Mn_{0.04})_{1-x}W_xO_2$ (x = 0.0025, 0.005, 0.0075, 0.01, 0.0125, 0.015, 0.02) were synthesized at 700, 750, 800 and 850 °C. Two fundamental characteristics were systematically examined: the morphological evolution, covering primary particle size, and aspect ratio; and the structural properties, including cation disordering and the reversibility of phase transitions during cycling. Notably, the results indicate that electrochemical stability is only weakly correlated with grain morphology, whereas capacity fading exhibits a strong inverse relationship with the extent of Li^+/Ni^{2+} cation mixing. This study conclusively demonstrates that the beneficial effect of high-valence W^{6+} doping arises mainly from the stabilization of the host lattice through mitigation of cation disorder and irreversible phase transitions, rather than from morphological modifications. This finding revises the conventional emphasis on morphological alignment. Ultimately, the proposed mechanism, combined with a co-optimization strategy for dopant concentration and sintering temperature, establishes a generalized design principle for the development of next-generation ultra-high-nickel cathode materials.

2. Results and discussion

To systematically evaluate the influence of tungsten doping and sintering temperature on the electrochemical behavior of the cathodes, comprehensive performance metrics are presented in Fig. 1 and Table S1. Initial charge–discharge profiles at 0.05C (Fig. 1a–d) reveal distinct differences in specific capacity and Coulombic efficiency. At 700 °C, the undoped N92-700 delivers a discharge capacity of 236.0 mAh g^{-1} with a Coulombic efficiency of 93.74%. Introduction of a low tungsten concentration, as in N92-W0.25-700, yields a comparable capacity of 231.8 mAh g^{-1} and a marginally decreased Coulombic efficiency of 92.91%, whereas higher doping levels, such as in N92-W1-700, lead to capacity reduction. When the sintering temperature is raised to 750 °C, optimally doped cathodes also demonstrate acceptable performance. Specifically, N92-W0.25-750 achieves a discharge capacity of 229.0 mAh g^{-1} and a Coulombic efficiency of 93.73%, outperforming the undoped N92-750, which exhibits 216.9 mAh g^{-1} and 93.11% efficiency. At 800 °C, where cation mixing becomes more pronounced, the undoped N92-800 shows degraded performance, with a capacity of 227.4 mAh g^{-1} and Coulombic efficiency of 90.04%. In contrast, N92-W0.75-800 attains a high capacity of 244.3 mAh g^{-1} and a Coulombic efficiency of 94.04%, indicating that an appropriate amount of W doping alleviates high-temperature degradation. Even under the severe sintering condition of 850 °C, the undoped N92-850 suffers from substantial structural deterioration, yielding only 209.7 mAh g^{-1} and 88.04% Coulombic efficiency, while W-doped cathodes such as N92-W1-850 maintain a higher capacity of 226.9 mAh g^{-1} and Coulombic efficiency of 93.23%, confirming that tungsten doping can extend the lithiation temperature range.

Cycling stability tests conducted at 1C (Fig. 1e–h) reveal pronounced differentiation in cycle life across sintering temperatures and doping levels. At 700 °C, the undoped N92-700 exhibits the highest capacity retention of 76.98%,

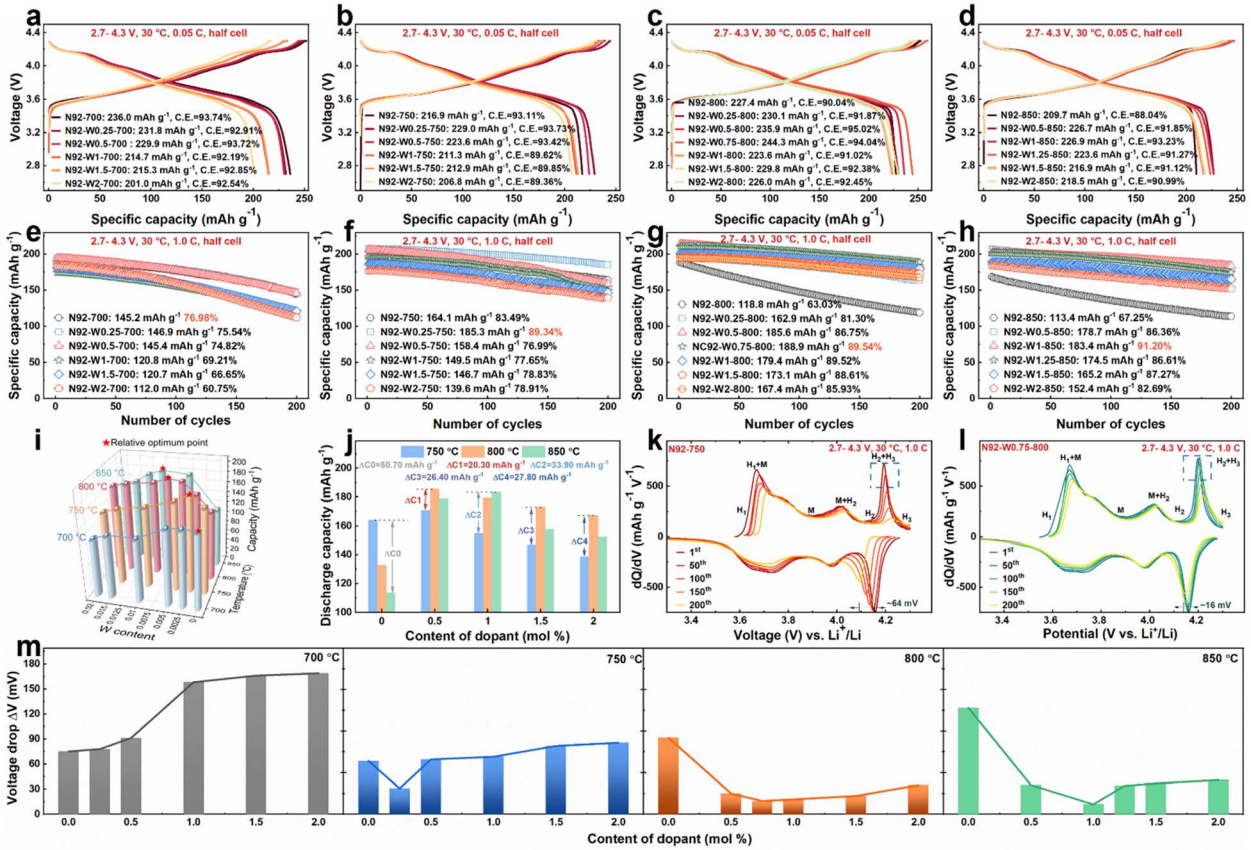

Fig. 1 (a–d) Galvanostatic charge–discharge profiles of half-cells at 0.05C (voltage range: 2.7–4.3 V, 30 °C). (e–h) Cycling stability of half-cells at 1C. (i) Radar chart and column plot quantifying the correlation among temperature, W dopant content, and discharge capacity to identify relative optimum conditions. (j) Bar graph comparing discharge capacities of cathodes with varying dopant contents at different temperatures. (k and l) Differential capacity (dQ/dV) curves of selected cathodes during cycling. (m) Voltage drop analysis of cathodes at different temperatures and dopant contents.

corresponding to a retained capacity of 145.2 mAh g^{-1} after 200 cycles. Cathodes with W doping all show decreased cycling stability. As the sintering temperature rises, the doped cathodes begin to exhibit better cycling performance than the pristine cathode. At 750 °C, N92-W0.25-750 delivers the best performance, retaining 185.3 mAh g^{-1} after 200 cycles with 89.34% capacity retention, significantly surpassing the undoped N92-750, which retains 164.1 mAh g^{-1} with 83.49% retention. At 800 °C, the temperature reaches the common upper limit for Ni-rich cathode lithiation. However, all W-modified cathodes substantially exceed the performance of undoped N92-800, with N92-W0.75-800 demonstrating excellent cycling stability, retaining 188.9 mAh g^{-1} and 89.54% of its initial capacity. When the temperature is elevated to 850 °C, the undoped N92-850 suffers severe capacity degradation, retaining only 113.4 mAh g^{-1}, attributed to excessive cation mixing induced by overheating. Under the same conditions, W-doped cathodes again display a non-monotonic relationship with doping content, with optimal performance observed at 1.0 mol% W doping. Fig. 1i and S1 illustrate a systematic shift in the optimal tungsten doping concentration with increasing temperature: approximately 0.25 mol% at 750 °C, 0.75 mol% at 800 °C, and 1.0 mol% at 850 °C. This trend indicates that more severe high-temperature conditions necessitate higher doping levels to achieve structural stabilization. Fig. 1j further quantifies the thermal sensitivity, showing that within the temperature range of 750–850 °C, the undoped N92 cathode exhibits a substantial capacity fluctuation of 50.70 mAh g^{-1}. In contrast, W-doped cathodes demonstrate significantly suppressed variations, such as 20.30 mAh g^{-1} for N92-W0.5 and 26.40 mAh g^{-1} for N92-W1.5. These results confirm that tungsten doping effectively broadens the processing temperature window by enhancing structural tolerance to high-temperature sintering.

Differential capacity analysis was employed to evaluate the structural stability and reversibility of phase transitions, which are key factors governing capacity retention and voltage hysteresis. As shown in Fig. 1k and l, the N92-W0.75-800 cathode exhibited outstanding electrochemical reversibility, maintaining sharp redox peaks around 4.2 V even after 200 cycles. The associated discharge voltage polarization was merely 16 mV, substantially lower than the 64 mV observed for the undoped N92-750 cathode. Moderately doped cathodes (Fig. S2–S5), such as N92-W0.5-850 and N92-W0.5-750, also outperformed their undoped counterparts, with voltage polarizations of approximately 35 mV and 66 mV after 200 cycles, respectively. By contrast, excessively doped materials like N92-

W2-700 displayed severe peak broadening and a large voltage hysteresis of 169 mV, indicative of increased kinetic barriers and structural distortion. Fig. 1m summarizes the discharge plateau voltage drops across all tested materials, indicating that an optimal W doping level exists at each sintering temperature to minimize voltage fade. For instance, at 800 °C, the N92-W0.75 cathode achieved the smallest voltage drop, which is consistent with its excellent cycling reversibility presented in the differential capacity curves. This trend underscores the critical importance of optimizing the doping concentration to balance structural stability and electrochemical performance. Collectively, these results verify that appropriate tungsten doping stabilizes the host framework, suppresses structural degradation, and mitigates lattice strain during cycling, thereby reducing irreversible phase transitions, voltage decay, and capacity fading. To clarify the origin of these performance variations, the following sections explore the underlying factors from kinetic, morphological, and structural perspectives.

To understand the kinetic origins of the electrochemical performance differences resulting from W doping and sintering temperature, electrochemical impedance spectroscopy and galvanostatic intermittent titration technique measurements were performed. Fig. 2a displays Nyquist plots of cathodes at the 1st and 200th cycles, measured at 0.1C. These spectra were fitted using equivalent circuits to extract key parameters, including solid electrolyte interphase resistance, charge-transfer resistance, and Warburg impedance related to Li^+ diffusion (Fig. 2b and Table S2). In the pristine state, undoped N92 exhibited a strong dependence of impedance on sintering temperature. For instance, N92-850 showed a significantly high charge-transfer resistance of 152.00 Ω, attributed to severe cation mixing and structural disorder induced by higher sintering temperatures. In contrast, W-doped cathodes, particularly those with optimal doping levels, displayed substantially lower impedance. At 800 °C, N92-W0.75-800 exhibited an ultralow charge-transfer resistance of 21.82 Ω, approximately

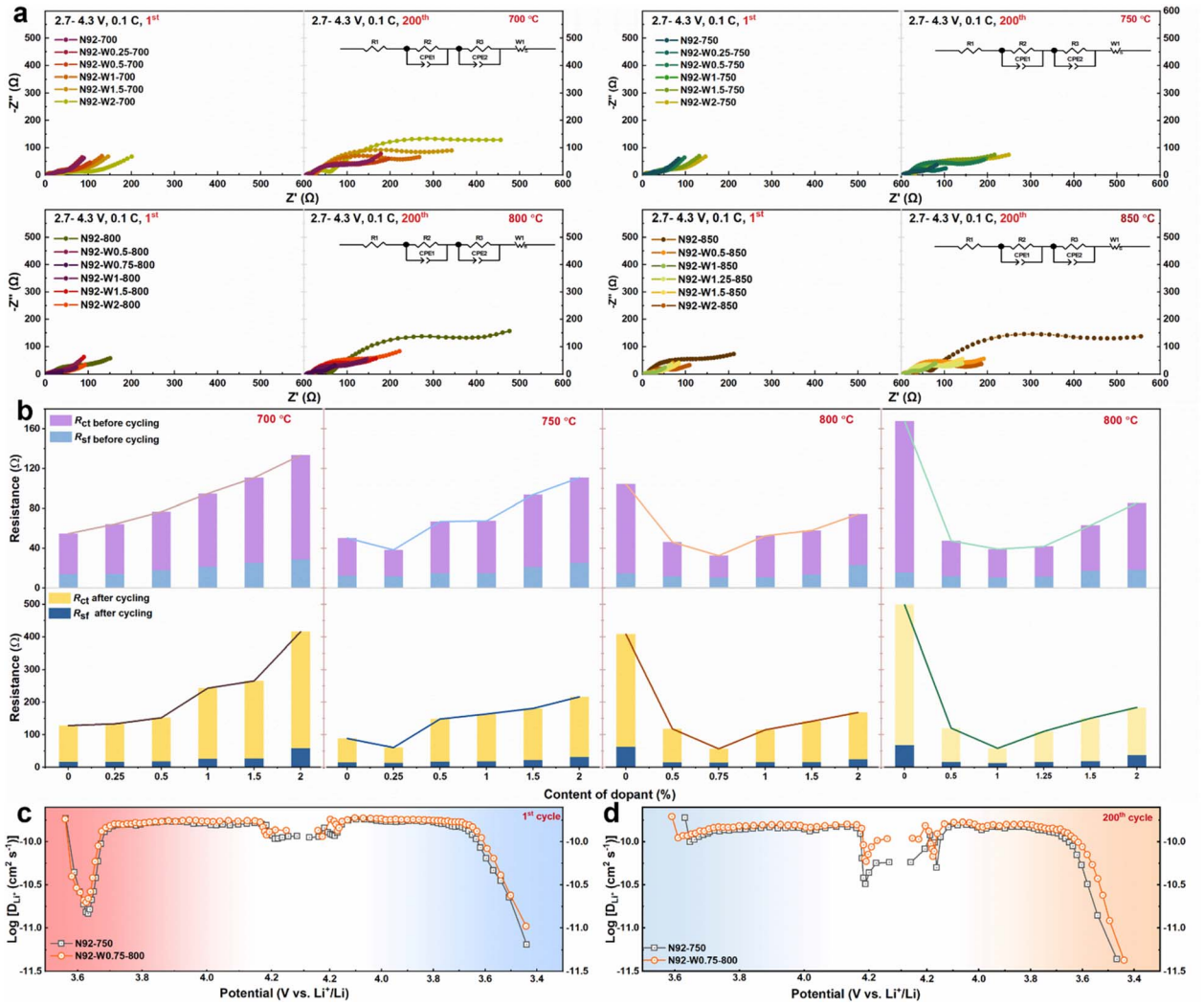

Fig. 2 (a) Electrochemical impedance spectroscopy (EIS) spectra of half-cells measured at 0.1C for the cathodes. (b) Bar graphs comparing charge transfer resistance (R_{ct}) and solid electrolyte interphase resistance (R_s) before and after cycling, as a function of W dopant content at different sintering temperatures. (c and d) Li^+ diffusion coefficient (D_{Li^+}) profiles as a function of voltage during the 200th cycle (c) and 1st cycle (d) for N92 and N92-W-0.75-800, calculated *via* the galvanostatic intermittent titration technique (GITT).

24% of that of the undoped N92-800 cathode, which had a charge-transfer resistance of 89.45 Ω. After 200 cycles, the undoped cathodes underwent a dramatic increase in impedance. The charge-transfer resistance of N92-700 increased from 40.78 Ω to 111.19 Ω, while that of N92-850 rose sharply to 431.3 Ω, indicating degradation of the solid electrolyte interphase and interfacial instability. In marked contrast, W-doped cathodes maintained significantly better resistance stability. The optimally doped N92-W0.75-800 showed only a moderate increase in charge-transfer resistance, from 21.82 Ω to 41.99 Ω, confirming the role of W in stabilizing the electrode–electrolyte interface. As shown in Fig. 2b, each sintering temperature corresponds to an optimal W-doping level that minimizes the impedance. Specifically, a clear correlation was observed between the optimal W-doping level and sintering temperature. The optimal doping concentration progressed from ~0 mol% at 700 °C, to 0.25 mol% at 750 °C, and 0.75 mol% at 800 °C, with the latter composition demonstrating the lowest impedance. At the highest temperature of 850 °C, the optimum was 1.0 mol%. This finding underscores the synergistic effect between W doping and sintering temperature in promoting charge-transfer kinetics. GITT measurements were performed to compare the Li^+ diffusion coefficients of the optimally performing undoped N92-750 and W-doped N92-W0.75-800 cathodes, as shown in Fig. 2c and d. This comparison was designed to evaluate the intrinsic kinetic advantages of W doping under respective optimal sintering conditions. In the pristine state, N92-W0.75-800 already exhibited a higher Li^+ diffusion coefficient than N92-750, indicating that W doping facilitates bulk Li^+ transport. After cycling, both materials showed a reduction in diffusion coefficients due to structural degradation; however, the W-doped cathode retained significantly higher Li^+ diffusivity. These results demonstrate that W doping not only improves initial Li^+ mobility but also helps preserve Li^+ transport pathways during long-term cycling. Combined with the EIS analysis, the GITT findings confirm that moderate W doping reduces charge-transfer resistance, stabilizes the interfacial structure, and enhances Li^+ diffusion kinetics. These observed improvements prompted further investigation into the roles of morphology and crystal structure.

While the kinetic data strongly suggest a bulk-stabilization mechanism, the extensively reported correlation between performance and morphology necessitates a rigorous examination of microstructural evolution. As shown in Fig. S8 and S9, although the calcination temperature had a minor influence on secondary particle size and sphericity, it strongly influenced the morphology of the primary particles. In the undoped N92, the primary particle size increased significantly with increasing temperature. Above 750 °C, the initially elongated primary particles transformed into more equiaxed shapes, a transition driven by enhanced atomic diffusion and grain coalescence under high-temperature conditions. In contrast, W doping led to considerable refinement of the primary particles compared to undoped cathodes processed at the same temperature. This refining effect became more pronounced with higher W concentrations. Although elevated temperatures still promoted grain growth in W-doped cathodes, the degree of coarsening was significantly suppressed relative to undoped N92. For example, the primary particles in N92-W1-850 were similar in size to those in undoped N92-700. Cross-sectional SEM images (Fig. 3a and S10) demonstrate that higher lithiation temperatures resulted in coarsening across all cathodes. N92 synthesized at 700 °C exhibited fine, acicular primary particles, whereas N92 synthesized at 750 °C developed larger, equiaxed grains. In comparison, W-doped cathodes maintained a refined needle-like morphology, an effect that intensified with increasing W content.

Quantitative analysis of primary particles, presented in Fig. 3b–e and S11, shows that cathodes lithiated at higher temperatures exhibited broadly distributed and irregular primary particle dimensions. In contrast, those synthesized at lower temperatures displayed reduced length and width values along with narrower size distributions. Under identical temperature conditions, W-doped materials further reduced particle size and narrowed the distribution. Notably, N92-W1-850 possessed finer and more uniform primary particles than both N92-W0.75-800 and undoped N92-750, as illustrated in Fig. 3e. Additional statistical analysis provided in Fig. S12 offers further quantification of the morphological regulation induced by W doping. Undoped N92 underwent significant thermal coarsening between 700 and 800 °C (Fig. S12a). The relative increase in particle width, with $\Delta W/W$ approximately 3.45, substantially exceeded the increase in length, where $\Delta L/L$ was about 0.72, indicating a trend toward isotropic particle growth. In W-doped cathodes such as N92-W1, coarsening was suppressed, with $\Delta W/W$ approximately 1.52 and $\Delta L/L$ approximately 0.50, effectively restraining width expansion and mitigating isotropic growth. At a fixed lithiation temperature, the aspect ratio, L/W, increased with higher W content. N92-W1 maintained a significantly larger L/W ratio compared to both N92-W0.5 and undoped N92, as shown in Fig. S12b, confirming that tungsten favors one-dimensional growth and helps preserve the needle-like morphology of primary particles. A direct comparison between undoped N92 and N92-W1 in Fig. S12c highlights the refining effect of W doping. The primary particle width in N92-W1-850 was only about one-third of that in the undoped cathode, with markedly reduced dimensional variation. The temperature-dependent evolution of the L/W ratio, shown in Fig. S12d, further emphasizes the stabilizing influence of W on particle morphology. Although all cathodes exhibited a decrease in L/W with increasing temperature, reflecting a general trend toward equiaxed grains, W-doped cathodes consistently maintained higher aspect ratios across the temperature range. For instance, N92-W1 retained a relatively high L/W at 850 °C, whereas undoped N92 had transitioned to a predominantly equiaxed structure. Collectively, W doping effectively suppresses temperature-induced grain coarsening, particularly along the width direction, and enhances anisotropic growth, resulting in refined and uniform needle-like primary particles. While these morphological improvements are beneficial, their weak correlation with electrochemical outcomes necessitates a deeper investigation into the crystal structure, specifically the role of cation ordering.

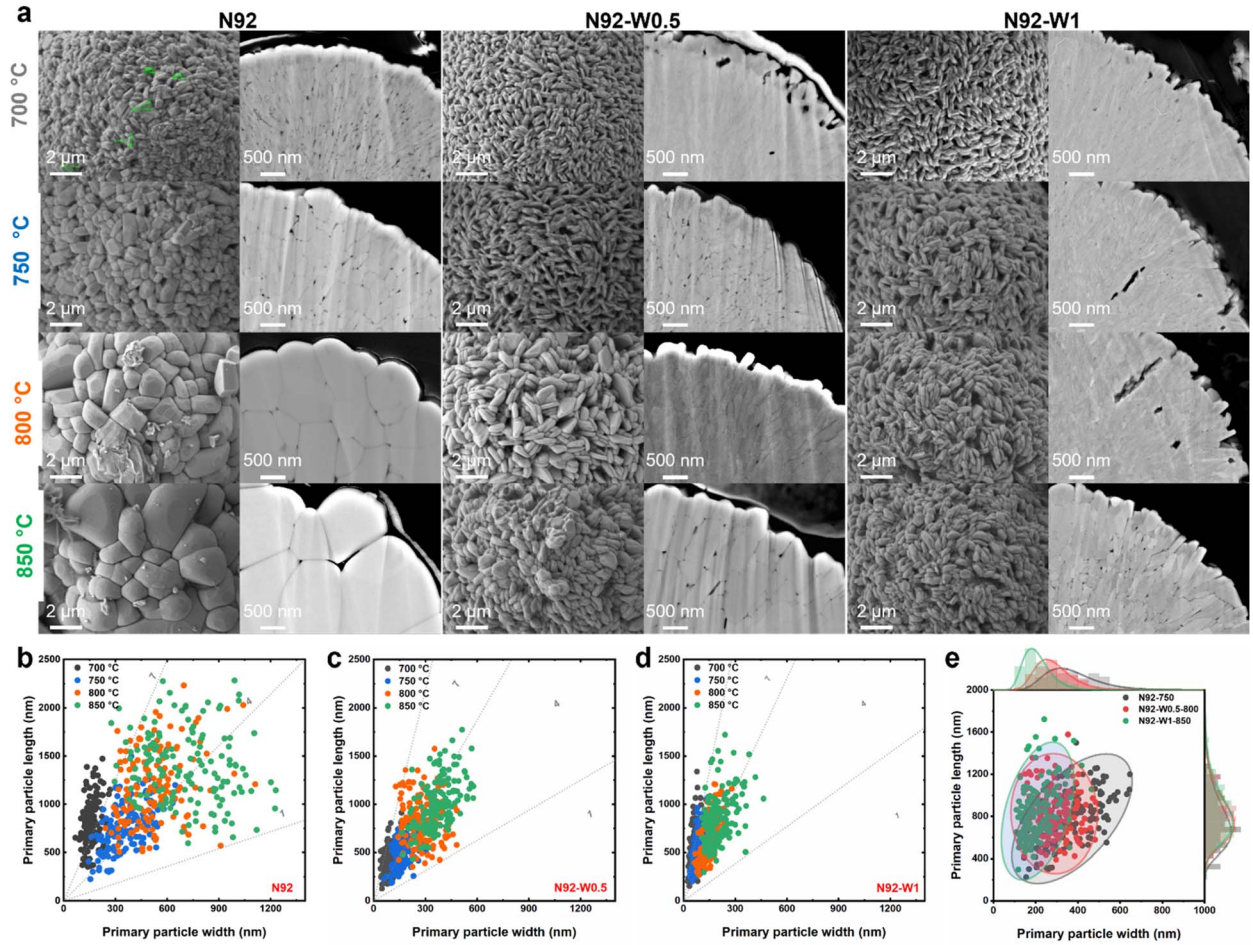

Fig. 3 (a) Scanning electron microscopy (SEM) images showing the surface (left, scale bar: 2 μm) and cross-sectional (right, scale bar: 500 nm) morphologies of N92, N92-W0.5, and N92-W1 cathodes sintered at 700 °C, 750 °C, 800 °C, and 850 °C. (b–d) Scatter plots of primary particle length *vs.* width for N92 (b), N92-W0.5 (c), and N92-W1 (d) cathodes at various sintering temperatures. (e) Combined distribution and kernel density estimation of primary particle length *vs.* width for selected cathodes (N92-750, N92-W0.5-800, N92-W1-850).

To systematically elucidate the synergistic effects of tungsten doping and calcination temperature on the structural characteristics of cathodes, comprehensive X-ray diffraction analyses with Rietveld refinement were conducted (Fig. S13–S20). All diffraction patterns confirm the formation of a well-defined layered α-$NaFeO_2$-type structure (space group $R\bar{3}m$) without detectable impurity phases, indicating successful incorporation of W^{6+} into the host lattice. The intensity ratio I_{003}/I_{104}, a critical indicator of structural ordering influenced by both Li^+/Ni^{2+} cation mixing and crystallographic preferential orientation, exhibits strong dependence on doping concentration and calcination temperature. As shown in Fig. 4a and Table S3, undoped cathodes display a marked decline in I_{003}/I_{104} with increasing temperature. For instance, N92-800 shows a ratio of only 1.10, accompanied by high cation mixing (6.41%) and large crystallite size (1157.6 nm), indicating that elevated temperatures exacerbate cation disorder and disrupt crystallite orientation. In contrast, W-doped cathodes demonstrate significantly enhanced structural stability. Optimal doping effectively mitigates cation disorder. Notably, N92-W0.75-800 achieves an I_{003}/I_{104} ratio of 1.27 with minimal cation mixing (2.06%), underscoring the role of W in preserving structural integrity. Systematic evaluation indicates that the optimal doping level increases with calcination temperature. Specifically, the optimal doping concentration is 0.25 mol% at 750 °C, 0.75 mol% at 800 °C, and 1.0 mol% at 850 °C. This trend is attributed to the increased demand for lattice stabilization under higher temperature conditions. Rietveld refinement confirms that W doping at appropriate temperature systematically reduces Li^+/Ni^{2+} cation mixing, as evidenced by the decrease in cation mixing from 3.6% in N92-800 to 2.1% in N92-W0.75-800. Lattice parameter evolution and peak shift analysis (Fig. S21) further reveal that W^{6+} incorporation induces contraction along both the *a*- and *c*-axes, enhancing structural coherence and suppressing phase transitions during cycling.

To monitor the structural evolution in real time during the synthesis process, *in situ* XRD analysis was conducted under isothermal conditions, first at 750 °C for 5 hours and then at 800 °C for an additional 5 hours. As shown in Fig. 4b, the undoped N92 cathode exhibited a steady increase in the intensities of the (003) and (104) peaks at 750 °C, suggesting progressive crystallization. However, upon transition to 800 °C,

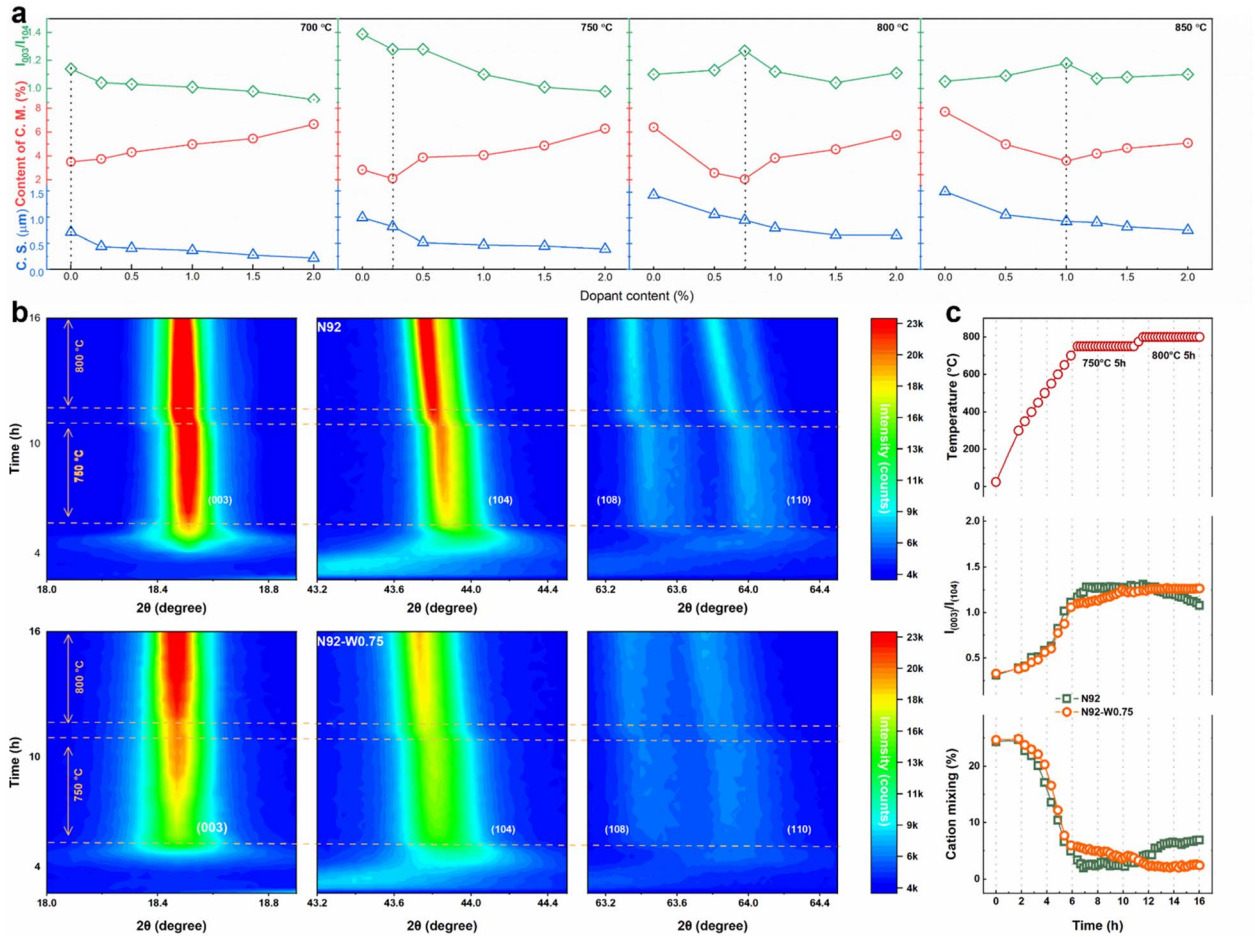

Fig. 4 (a) Plots of cation mixing content (C. M.), crystallite size (C. S.), and I_{003}/I_{104} as a function of W dopant content at sintering temperatures of 700 °C, 750 °C, 800 °C, and 850 °C. (b) *In situ* XRD contour maps monitoring the evolution of (003), (104), (108), and (110) peaks during sintering for N92 and N92-W0.75. (c) Temperature profile (top), intensity ratio (I_{003}/I_{104}, middle), and cation mixing evolution (bottom) during sintering for N92 and N92-W0.75.

the structure underwent severe degradation, manifested by noticeable peak shifting and broadening of the (003) and (104) reflections, indicative of structural collapse and loss of layered ordering. In contrast, the W-doped N92-W0.75 cathode demonstrated exceptional structural stability throughout the thermal treatment. Both the (003) and (104) peak intensities increased progressively at 750 °C and were maintained at 800 °C. Furthermore, the (108) and (110) peaks, which are sensitive to both cation ordering and layer stacking, remained clearly resolved at 800 °C, indicating the retention of a highly ordered layered structure. Quantitative refinement results are summarized in Fig. 4c.

The undoped cathode displayed a sharp increase followed by a rapid decrease in the I_{003}/I_{104} intensity ratio upon heating to 800 °C, coupled with a pronounced increase in Li^+/Ni^{2+} cation mixing from approximately 2.7% to over 4.0%. This behavior reflects significant crystallinity loss and enhanced cation disordering at elevated temperatures. On the other hand, N92-W0.75 maintained a consistently high I_{003}/I_{104} ratio and a low cation mixing level of approximately 2.3% throughout the entire process, including the 800 °C segment. The preserved intensity ratio and suppressed cation disorder underscore the efficacy of W-doping in stabilizing the host structure against thermal degradation. It is important to note that the I_{003}/I_{104} ratio is influenced not only by cation mixing but also by the degree of preferred crystallographic orientation (aspect ratio). In the undoped material, high temperature exacerbates both cation disorder and deterioration in grain orientation, collectively contributing to the decline in the I_{003}/I_{104} ratio. For the W-doped cathode, however, the doping effect suppresses cation disordering even as temperature increases, while the aspect ratio remains largely unaffected, thereby sustaining a high I_{003}/I_{104} value. These results clearly demonstrate that W doping significantly enhances the thermal stability and structural integrity of Ni-rich layered cathodes, effectively raising the maximum allowable lithiation temperature by suppressing cation disorder.

To elucidate the differences in structural evolution during electrochemical cycling, *in situ* X-ray diffraction was performed on pristine N92-750, N92-W0.25-750, N92-W0.5-800, and N92-W1-850 cathodes over the first cycle between 2.7 and 4.3 V at 0.05C. Fig. 5a–d display contour maps of key reflections—(003), (101), (104), (108), and (110)—superimposed with the corresponding charge/discharge profiles. In all cathodes, the (003)

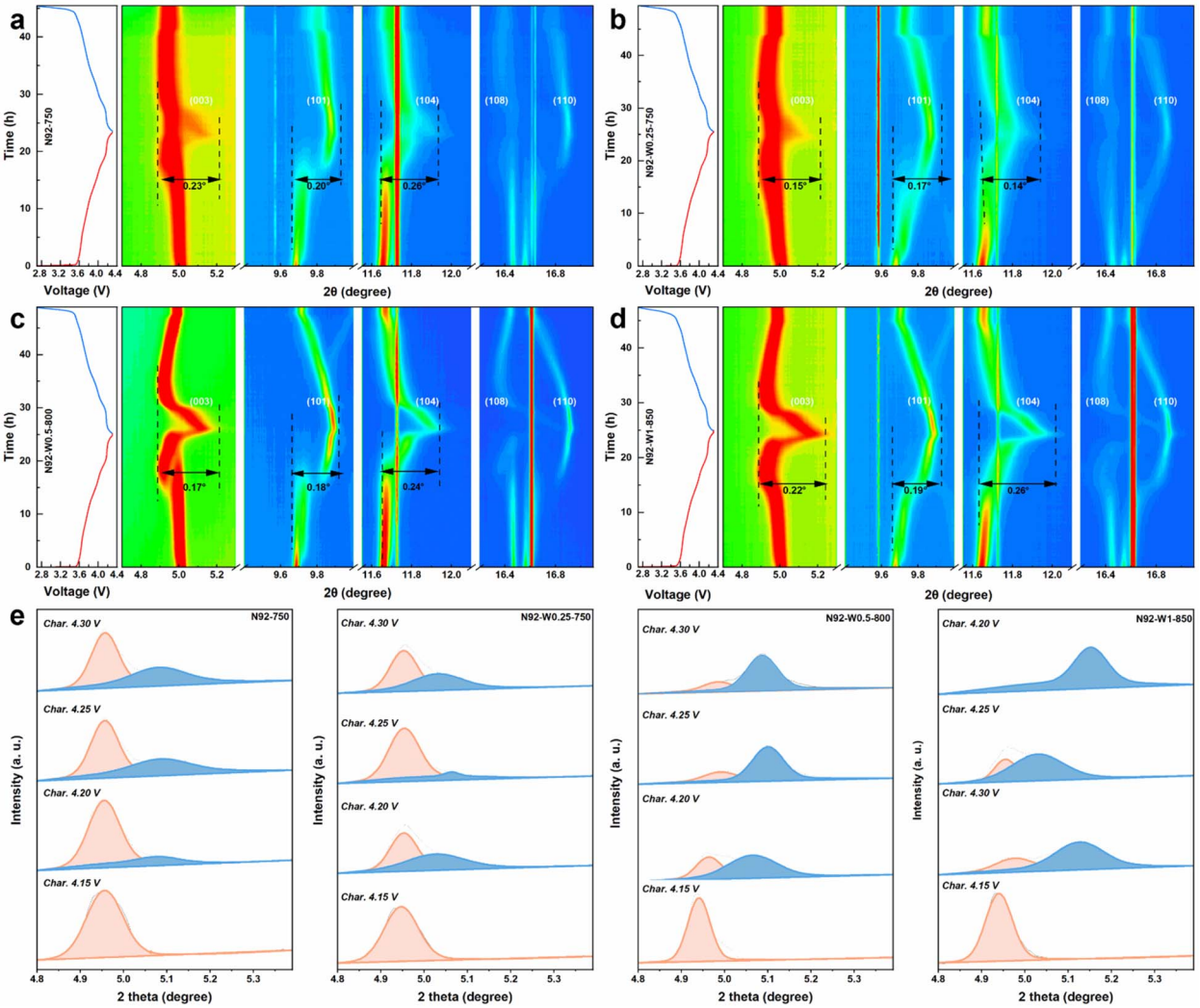

Fig. 5 (a–d) Contour maps of XRD peaks as a function of time and 2θ angle, coupled with voltage profiles (left) for N92-750 (a), N92-W0.25-750 (b), N92-W0.5-800 (c), and N92-W1-850 (d). (e) Deconvolution of XRD peaks around 4.8°–5.3° 2θ at different charging voltages for selected cathodes.

peak shifts to lower 2θ angles during charging up to approximately 4.15 V, indicating *c*-axis expansion due to Li^+ extraction, and then shifts back toward higher angles upon further charging. The (110) peak, reflecting *a*-axis variations, exhibits relatively minor shifts. However, distinct differences in structural evolution are evident between the pristine and W-modified cathodes. For N92-750, the (003) peak intensity attenuates abruptly above approximately 4.15 V and reappears at a higher angle characteristic of the H3 phase, signaling a discontinuous phase transition. In contrast, W-modified cathodes show a continuous shift of the (003) reflection toward higher angles without significant intensity loss or peak splitting, indicating a more coherent and homogeneous structural transition. Quantitative analysis of the H2 → H3 phase transition kinetics *via* deconvolution of the (003) peak (Fig. 5e–h) further reveals that W-modified cathodes, particularly N92-W1-850, achieve nearly complete conversion to the H3 phase by 4.30 V, whereas the pristine N92-750 retains a substantial H2-phase fraction. Mechanistically, reduced cation mixing underpins this coherent transition by minimizing local lattice strain, which would otherwise serve as nucleation sites for discontinuous H2–H3 phase changes. Less cation mixing allows the layered structure to maintain greater structural integrity, thereby enabling reversible expansion and contraction along the *c*-axis during lithium-ion intercalation and deintercalation. This reduction in local strain lowers the kinetic barriers for phase transitions, thus preventing splitting of the (003) diffraction peak, and directly decreases voltage hysteresis by reducing energy dissipation associated with irreversible structural damage.

Post-cycling cross-sectional SEM characterization (Fig. 6a) reveals distinct structural evolution across the cathode variants after 200 cycles at 1C. For the undoped N92-750 cathode, severe mechanical degradation is observed after prolonged cycling, manifested as extensive intergranular cracking and distinct particle fragmentation. In contrast, the W-doped N92-W0.25-750 and N92-W0.75-800 cathodes maintain substantially enhanced structural integrity, where intergranular defects are

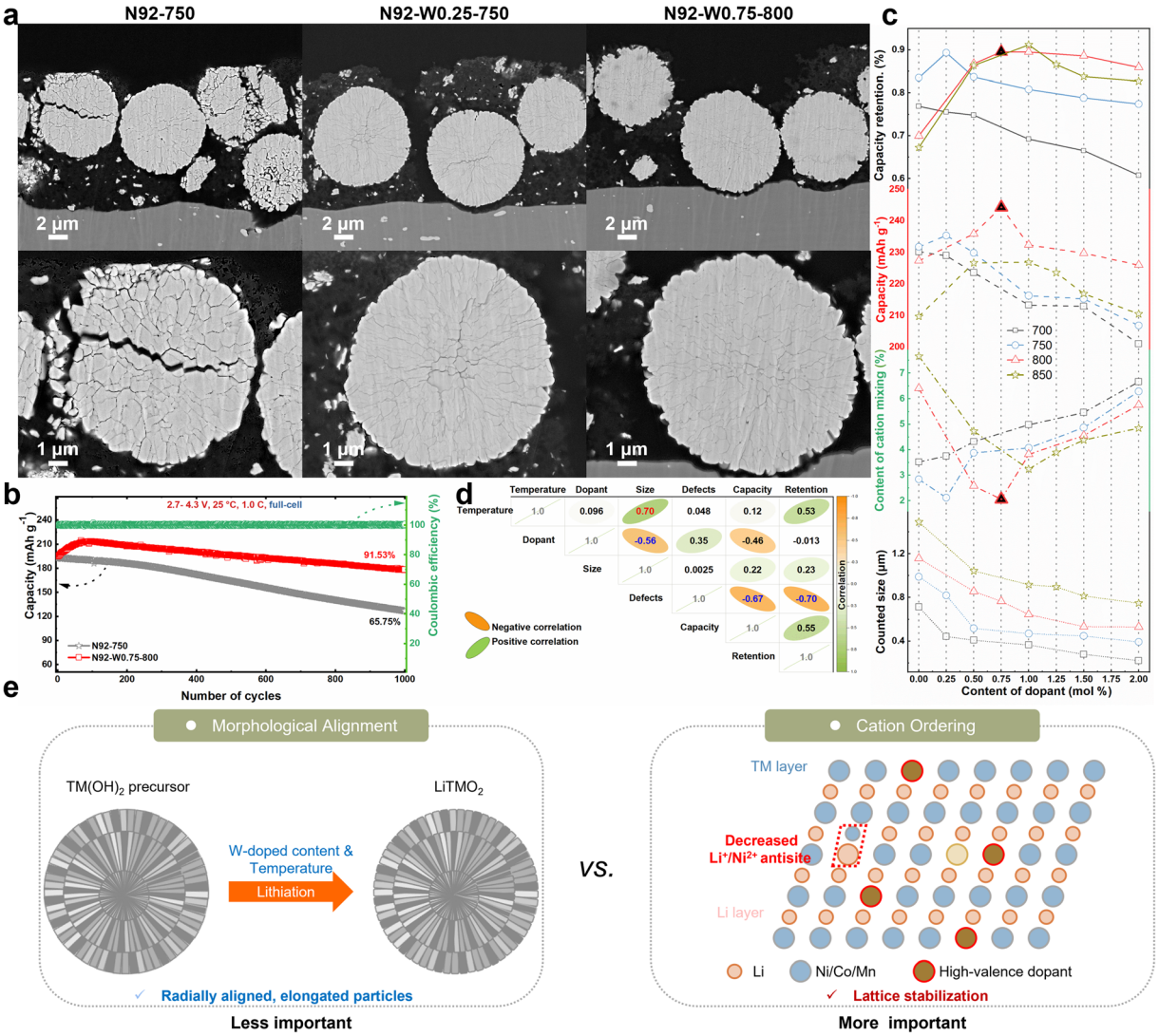

Fig. 6 (a) Cross-sectional SEM images of N92-750, N92-W0.25-750, and N92-W0.75-800. (b) Long-term cycling performance and Coulombic efficiency of full cells for N92-750 and N92-W0.75-800. (c) Multi-parameter correlation curves illustrating the dependence of capacity retention, discharge capacity, cation mixing content, and primary particle size on W dopant content at different sintering temperatures. (d) Correlation heatmap quantifying the relationships between temperature, dopant content, particle size, defects, discharge capacity, and capacity retention. (e) Schematic illustration comparing the roles of morphological alignment and cation ordering in enhancing stability.

largely alleviated and no obvious particle breakdown is detected. This improved mechanical robustness is attributed to W-induced structural densification, which inhibits the initiation and propagation of microcracks during repeated lithium-ion intercalation and deintercalation processes. Electrochemical performance was further evaluated in full cells with graphite anodes (Fig. 6b). The results demonstrate significantly improved cycling stability for the optimally doped N92-W0.75-800 cathode. When cycled between 2.7 V and 4.2 V at 25 °C and a rate of 1.0C, this material retained 91.53% of its initial capacity after 1000 cycles. By comparison, the undoped sample N92-750 exhibited a substantially lower capacity retention of only 65.75% under identical testing conditions. Moreover, compared to conventional Ni-rich cathodes, materials synthesized *via* simultaneous optimization of dopant concentration and lithiation temperature exhibit competitive initial capacity, improved rate capability, and superior cycling retention (Fig. S22 and Table S4).

To elucidate the intrinsic relationships between electrochemical performance and material characteristics, a systematic investigation was carried out, encompassing morphological and structural properties as functions of synthesis parameters. As illustrated in Fig. 6c, the evolution of key electrochemical metrics (specific capacity, capacity retention) and material descriptors (cation mixing extent, grain size) with synthesis parameters is comprehensively presented. Notably, cation mixing exhibits a strong inverse correlation with both specific capacity and cycling stability, featuring an initial decrease followed by an increase. Cathodes with minimal cation mixing, which is achieved at a sintering-temperature-specific optimal dopant concentration, deliver the highest reversible capacities and most stable cycling performance. In contrast, grain size

decreases monotonically with increasing dopant content and shows no consistent correlation with electrochemical properties. For instance, N92-W0.75-800 exhibits the lowest cation mixing, corresponding to the highest specific capacity and reasonably good capacity retention, even without the most radially elongated grain morphology. Conversely, materials doped with 1.5–2 mol% W and synthesized at 700–750 °C possess distinctly radially aligned and elongated grains but suffer from significant cation mixing, resulting in inferior specific capacity and cycling stability. These trends corroborate previous findings that cation disorder intensifies under either low dopant content with high temperature or high dopant content with low temperature, underscoring the detrimental impact of cation disorder on electrochemical performance. Furthermore, Fig. 6d presents a heatmap of Pearson correlation coefficients, quantifying the statistical associations among synthesis parameters, morphological/structural descriptors (grain size, defect content), and electrochemical metrics. The heatmap confirms that capacity retention is only weakly correlated with morphological parameters like grain size, whereas cation mixing displays a strong negative correlation with both specific capacity and cycling stability. Mechanistically, reduced cation mixing enhances H2–H3 phase transition stability not only by suppressing strain-induced discontinuous phase transitions but also by stabilizing transition metal–oxygen (TM–O) bonds. Strengthened TM–O bonds mitigate oxygen loss during cycling, thereby alleviating cumulative lattice damage. These effects collectively improve voltage retention, aligning with the observed trend: optimal W doping, which minimizes cation mixing, correlates with superior voltage hysteresis performance and H2–H3 phase transition reversibility. Coupled with the schematic in Fig. 6e, these findings illustrate that cation ordering plays a more decisive role in enhancing electrochemical performance than morphological control *via* radial grain alignment. Morphological control, achieved by modulating W dopant concentration and lithiation temperature during the transformation of transition metal hydroxide precursors into lithium transition metal oxides, induces radially aligned elongated particles. However, this structural alignment exerts only a limited effect on electrochemical performance. In contrast, cation ordering facilitates lattice stabilization: the incorporation of high-valence W dopants at appropriate temperature mitigates Li^+/Ni^{2+} antisite mixing between transition metal and lithium layers, thereby more effectively suppressing structural degradation in Ni-rich layered oxides. This study demonstrates that optimizing cation ordering is more critical than merely modulating morphology for enhancing the electrochemical performance of Ni-rich layered oxides. This insight provides a clear directive for the rational design of high-performance cathode materials.

3. Conclusions

Based on a systematic investigation of W^{6+}-doped $LiNi_{0.92}Co_{0.04}Mn_{0.04}O_2$ across various doping concentrations and sintering temperatures, this study demonstrates that cation ordering, rather than morphological alignment, serves as the dominant mechanism for enhancing structural and electrochemical stability. While increased lithiation temperature generally degrades the radially aligned microstructure in both undoped and doped materials, the introduction of W significantly raises the thermal stability threshold, preserving the radial particle morphology even under harsh sintering conditions. Correlation analyses reveal that electrochemical performance exhibits only a weak dependence on grain orientation and size, whereas a strong negative correlation exists between Li^+/Ni^{2+} cation mixing and key metrics such as specific capacity and cycling retention. The novelty and generalizability of our work lie in establishing the "cation ordering over morphology" paradigm. This insight provides a universal design principle that transcends the specific W-doped system studied here, offering a critical guideline for the co-optimization of future high-energy cathodes, including Ni-rich and other layered oxide varieties.

Author contributions

Shuo Wang: investigation, data curation, validation, writing – original draft. Siqi Chen: investigation, methodology, formal analysis. Xiaohong Liu: conceptualization, data curation, writing – original draft, supervision, funding acquisition. Guilin Feng: resources, investigation. Bin Zhang: resources. Wangyan Xing: resources. Yao Xiao: writing – review & editing, supervision. Hao Liu: methodology, characterization, writing – review & editing. Wei Xiang: conceptualization, project administration, data curation, writing – original draft & finalization, supervision, funding acquisition.

Conflicts of interest

There are no conflicts to declare.

Data availability

Essential data are fully provided in the main text and supplementary information (SI). Supplementary information: comprehensive experimental details and supporting data. This includes the detailed synthesis procedure for cathodes across a range of doping concentrations and sintering temperatures; full characterization methods (XRD, SEM, *etc.*) and electrochemical testing protocols. It provides additional electrochemical performance figures (dQ/dV profiles, rate capability), extensive morphological analysis (SEM images, primary particle statistics), structural characterization data (full XRD patterns, Rietveld refinement results, lattice parameter evolution), and corresponding numerical data tables (electrochemical performance, EIS parameters, structural parameters). A comparative performance table benchmarking the optimized cathode against previously reported high-valence doped Ni-rich materials is also included. These data collectively support the findings and discussions presented in the main manuscript. See DOI: https://doi.org/10.1039/d5sc09030j.

Acknowledgements

This work was financially supported by a project from the National Natural Science Foundation of China (22578037 and 22508025), and by the Sichuan Science and Technology Program (2025NSFSC2060 and 2025ZNSFSC0967). Especially, we thank Ceshigo (https://www.ceshigo.com/) and Zhinanzhen (https://www.shiyanjia.com/) for characterization measurements.

References

1 G. T. Park, H. H. Ryu, N. Y. Park, S. B. Lee and Y. K. Sun, Single-Crystal vs Polycrystalline Cathodes for Lithium-Ion Batteries, *Chem. Rev.*, 2025, **125**, 9930–10000.

2 J. Zheng, S. Zhao, W. Guan, S. Liao, T. Zeng, S. Zhang, Z. Yue, S. Fang, N. Zhou, Y. Jiang and Y. Li, Tungsten-doping enables excellent kinetics and high stability of cobalt-free ultrahigh-nickel single-crystal cathode, *Energy Storage Mater.*, 2025, **78**, 104251.

3 J. Peng, J. Yang, S. Hao, Y. Li, S. Liu, S. Jiang, S. Sun and Z. He, Enhanced mechanical property promote high stability of single-crystal Ni-rich cathode at 4.5 V, *Energy Storage Mater.*, 2025, **77**, 104199.

4 J. X. Meng, L. S. Xu, Q. X. Ma, M. Q. Yang, Y. Z. Fang, G. Y. Wan, R. H. Li, J. J. Yuan, X. K. Zhang, H. J. Yu, L. L. Liu and T. F. Liu, Modulating Crystal and Interfacial Properties by W-Gradient Doping for Highly Stable and Long Life Li-Rich Layered Cathodes, *Adv. Funct. Mater.*, 2022, **32**, 2113013.

5 N. Zaker, C. X. Geng, D. Rathore, I. Hamam, N. Chen, P. H. Xiao, C. Y. Yang, J. R. Dahn and G. A. Botton, Probing the Mysterious Behavior of Tungsten as a Dopant Inside Pristine Cobalt-Free Nickel-Rich Cathode Materials, *Adv. Funct. Mater.*, 2023, **33**, 2211178.

6 Q. M. Zhang, Q. Deng, W. T. Zhong, J. Li, Z. M. Wang, P. Y. Dong, K. V. Huang and C. H. Yang, Tungsten Boride Stabilized Single-Crystal $LiNi_{0.83}Co_{0.07}Mn_{0.1}O_2$ Cathode for High Energy Density Lithium-Ion Batteries: Performance and Mechanisms, *Adv. Funct. Mater.*, 2023, **33**, 2301336.

7 D. Rathore, M. Garayt, Y. L. Liu, C. X. Geng, M. Johnson, J. R. Dahn and C. Y. Yang, Preventing Interdiffusion during Synthesis of Ni-Rich Core-Shell Cathode Materials, *ACS Energy Lett.*, 2022, **7**, 2189–2195.

8 H. Zhu, Z. Wang, L. Chen, Y. Hu, H. Jiang and C. Li, Strain Engineering of Ni-Rich Cathode Enables Exceptional Cyclability in Pouch-Type Full Cells, *Adv. Mater.*, 2023, **35**, 2209357.

9 N. Y. Park, G. Cho, S. B. Kim and Y. K. Sun, Multifunctional Doping Strategy to Develop High-Performance Ni-Rich Cathode Material, *Adv. Energy Mater.*, 2023, **13**, 2204291.

10 N. Y. Park, H. H. Ryu, L. Y. Kuo, P. Kaghazchi, C. S. Yoon and Y. K. Sun, High-Energy Cathodes via Precision Microstructure Tailoring for Next-Generation Electric Vehicles, *ACS Energy Lett.*, 2021, **6**, 4195–4202.

11 U. H. Kim, S. B. Lee, N. Y. Park, S. J. Kim, C. S. Yoon and Y. K. Sun, High-Energy-Density Li-Ion Battery Reaching Full Charge in 12 min, *ACS Energy Lett.*, 2022, **7**, 3880–3888.

12 S. B. Lee, N. Y. Park, G. T. Park, U. H. Kim, S. J. Sohn, M. S. Kang, R. M. Ribas, R. S. Monteiro and Y. K. Sun, Doping Strategy in Developing Ni-Rich Cathodes for High-Performance Lithium-Ion Batteries, *ACS Energy Lett.*, 2024, **9**, 740–747.

13 F. Xin, H. Zhou, Y. Zong, M. Zuba, Y. Chen, N. A. Chernova, J. Bai, B. Pei, A. Goel, J. Rana, F. Wang, K. An, L. F. J. Piper, G. Zhou and M. S. Whittingham, What is the Role of Nb in Nickel-Rich Layered Oxide Cathodes for Lithium-Ion Batteries?, *ACS Energy Lett.*, 2021, **6**, 1377–1382.

14 G. T. Park, N. Y. Park, H. H. Ryu, H. H. Sun, J. Y. Hwang and Y. K. Sun, Nano-rods in Ni-rich layered cathodes for practical batteries, *Chem. Soc. Rev.*, 2024, **53**, 11462–11518.

15 X. M. Fan, Y. D. Huang, H. X. Wei, L. B. Tang, Z. J. He, C. Yan, J. Mao, K. H. Dai and J. C. Zheng, Surface Modification Engineering Enabling 4.6 V Single-Crystalline Ni-Rich Cathode with Superior Long-Term Cyclability, *Adv. Funct. Mater.*, 2022, **32**, 2109421.

16 Z. S. Dai, F. Wu, R. J. Chen and L. Li, High-Entropy Induces Self-Limiting and Controllable Surface Coherent Phase Achieving Exceptional Ah-Level Ni-Rich Co-Free Batteries, *ACS Nano*, 2025, **19**, 36739–36748.

17 G. Ko, S. Jeong, S. Park, J. Lee, S. Kim, Y. Shin, W. Kim and K. Kwon, Doping strategies for enhancing the performance of lithium nickel manganese cobalt oxide cathode materials in lithium-ion batteries, *Energy Storage Mater.*, 2023, **60**, 102840.

18 Z. Cui, X. Li, X. Bai, X. Ren and X. Ou, A comprehensive review of foreign-ion doping and recent achievements for nickel-rich cathode materials, *Energy Storage Mater.*, 2023, **57**, 14–43.

19 C. Geng, D. Rathore, D. Heino, N. Zhang, I. Hamam, N. Zaker, G. A. Botton, R. Omessi, N. Phattharasupakun, T. Bond, C. Yang and J. R. Dahn, Mechanism of Action of the Tungsten Dopant in $LiNiO_2$ Positive Electrode Materials, *Adv. Energy Mater.*, 2021, **12**, 2103067.

20 H. H. Ryu, K. J. Park, D. R. Yoon, A. Aishova, C. S. Yoon and Y. K. Sun, $LiNi_{0.9}Co_{0.09}W_{0.01}O_2$: A New Type of Layered Oxide Cathode with High Cycling Stability, *Adv. Energy Mater.*, 2019, **9**, 1902698.

21 J. F. Zheng, S. Q. Zhao, W. C. Guan, S. N. Liao, T. Zeng, S. R. Zhang, Z. H. Yue, S. Fang, N. G. Zhou, Y. Z. Jiang and Y. Li, Tungsten-doping enables excellent kinetics and high stability of cobalt-free ultrahigh-nickel single-crystal cathode, *Energy Storage Mater.*, 2025, **78**, 104251.

22 N. Y. Park, M. C. Kim, S. M. Han, G. T. Park, D. H. Kim, M. S. Kim and Y. K. Sun, Mechanism Behind the Loss of Fast Charging Capability in Nickel-Rich Cathode Materials, *Angew. Chem., Int. Ed.*, 2024, **63**, e202319707.

23 N. Y. Park, S. M. Han, J. H. Ryu, M. C. Kim, J. I. Yoon, J. H. Kim, G. T. Park, J. E. Frerichs, C. Erk and Y. K. Sun, Tailoring Primary Particle Size Distribution to Suppress Microcracks in Ni-Rich Cathodes via Controlled Grain Coarsening, *ACS Energy Lett.*, 2024, **9**, 3595–3604.

24 G. T. Park, S. B. Kim, J. I. Yoon, N. Y. Park, M. C. Kim, S. M. Han, D. H. Kim, M. S. Kim and Y. K. Sun, Unraveling the New Role of Manganese in Nano and Microstructural

Engineering of Ni-Rich Layered Cathode for Advanced Lithium-Ion Batteries, *Adv. Energy Mater.*, 2024, **14**, 2400130.
25 H. H. Ryu, H. W. Lim, G. C. Kang, N. Y. Park and Y. K. Sun, Long-Lasting Ni-Rich NCMA Cathodes via Simultaneous Microstructural Refinement and Surface Modification, *ACS Energy Lett.*, 2023, **8**, 1354–1361.
26 G. T. Park, S. B. Kim, B. Namkoong, J. H. Ryu, J. I. Yoon, N. Y. Park, M. C. Kim, S. M. Han, F. Maglia and Y. K. Sun, Intergranular Shielding for Ultrafine-Grained Mo-Doped Ni-Rich $LiNi_{0.96}Co_{0.04}O_2$ Cathode for Li-Ion Batteries with High Energy Density and Long Life, *Angew. Chem., Int. Ed.*, 2023, **62**, e202314480.
27 G. T. Park, S. M. Han, J. H. Ryu, M. C. Kim, D. H. Kim, M. S. Kim and Y. K. Sun, Opening a New Horizon for the Facile Synthesis of Long-Life Ni-Rich Layered Cathode, *ACS Energy Lett.*, 2023, **8**, 3784–3792.
28 G.-T. Park, N.-Y. Park, T.-C. Noh, B. Namkoong, H.-H. Ryu, J.-Y. Shin, T. Beierling, C. S. Yoon and Y.-K. Sun, High-performance Ni-rich $LiNi_{0.9-x}Co_{0.1}Al_xO_2$ cathodes via multi-stage microstructural tailoring from hydroxide precursor to the lithiated oxide, *Energy Environ. Sci.*, 2021, **14**, 5084–5095.
29 U.-H. Kim, G.-T. Park, B.-K. Son, G. W. Nam, J. Liu, L.-Y. Kuo, P. Kaghazchi, C. S. Yoon and Y.-K. Sun, Heuristic solution for achieving long-term cycle stability for Ni-rich layered cathodes at full depth of discharge, *Nat. Energy*, 2020, **5**, 860–869.
30 G. T. Park, B. Namkoong, S. B. Kim, J. Liu, C. S. Yoon and Y. K. Sun, Introducing high-valence elements into cobalt-free layered cathodes for practical lithium-ion batteries, *Nat. Energy*, 2022, **7**, 946–954.
31 W. Wang, Z. M. Xiao, J. X. Liu, X. Y. He, J. G. Wen, Y. N. Zhou, L. Cheng, B. Zhang, T. C. Liu, K. Amine and X. Ou, Surface Atomic Rearrangement with High Cation Ordering for Ultra-Stable Single-Crystal Ni-Rich Co-Less Cathode Materials, *Adv. Funct. Mater.*, 2024, **34**, 2409956.
32 X. Zhou, F. Hong, S. Wang, T. Zhao, J. Peng, B. Zhang, W. Fan, W. Xing, M. Zuo, P. Zhang, Y. Zhou, G. Lv, Y. Zhong, W. Hua and W. Xiang, Precision engineering of high-performance Ni-rich layered cathodes with radially aligned microstructure through architectural regulation of precursors, *eScience*, 2024, **4**, 100276.
33 S. Wang, X. Zhou, T. Zhao, J. Peng, Z. Bin, W. Xing, M. Zuo, P. Zhang, W. Fan, G. Lv, W. Hua and W. Xiang, Precise regulation of particle orientation for Ni-rich cathodes with ultra-long cycle life, *Nano Energy*, 2024, **129**, 110008.